Relativistic Cyclotron

Abstract This chapter introduces the AVF (azimuthally varying field), isochronous, relativistic cyclotron, and to the theoretical material needed for the simulation exercises. A brief reminder of the historical context is followed by further basic theoretical considerations leaning on the cyclotron concepts introduced in Chapter 3 and including

- Thomas focusing and the AVF cyclotron,
- positive focusing index,
- isochronous optics,
- separated sector cyclotrons,
- spin dynamics in an AVF cyclotron.

Simulation exercises use optical elements and keywords met earlier: the analytical field modeling DIPOLE, TOSCA in case using a field map is preferred, CAVITE to accelerate, SPNTRK to solve spin motion, FAISCEAU, FAISTORE, FIT, etc. The exercises further develop on radial and spiral sector magnets, edge focusing and flutter, isochronous optics, separated sector ring cyclotrons, and their modeling in DIPOLE, DIPOLES and other CYCLOTRON keyword capabilities.

Notations used in the Text

B; B_0	magnetic field; at a reference radius R_0
$\mathbf{B}$; B_R; B_θ; B_y	field vector; radial, azimuthal and axial components
$BR = p/q$; BR_0	magnetic rigidity; reference rigidity
C; C_0	closed orbit length, $C = 2\pi R$; reference, $C_0 = 2\pi R_0$
E	ion energy, $E = \gamma m_0 c^2$
EFB	effective Field Boundary
$\mathcal{F}$; F	azimuthal field form factor; flutter, $F = \left(\frac{<(\mathcal{F}-<\mathcal{F}>)^2>}{<\mathcal{F}>^2}\right)^{1/2}$
f_{rev}, f_{rf}	revolution and RF voltage frequencies
h	harmonic number, an integer, $h = f_{\mathrm{rf}}/f_{\mathrm{rev}}$
$k = \frac{R}{B}\frac{dB}{dR}$	geometric index, a global quantity
m; m_0; M	ion mass; rest mass; in units of MeV/c^2
$n = \frac{\rho}{B}\frac{dB}{d\rho}$	focusing index, a local quantity
$\mathbf{p}$; p_0	ion momentum vector; reference momentum
q	ion charge
R; R_0; R_E	average radius of equilibrium orbit; $R = C/2\pi$; $R(p = p_0)$; $R(E)$
$\mathcal{R}$	radial field form factor
RF	Radio-Frequency
s	path variable
T_{rev}, T_{rf}	revolution and accelerating voltage periods
v	ion velocity
V(t); $\hat{V}$	oscillating voltage; its peak value
x, x', y, y'	radial and axial coordinates $\left[(*)' = \frac{d(*)}{ds}\right]$
α	trajectory deviation, or momentum compaction
$\beta = v/c$; β_0; β_s	normalized ion velocity; reference; synchronous
$\gamma = E/m_0c^2$	Lorentz relativistic factor
Δp, δp	momentum offset
ε	wedge angle
ϵ_R	strength of a depolarizing resonance
ε_u	Courant-Snyder invariant (u : x, y, l), ...)
ζ	spiral angle of a spiral sector dipole EFB
θ	azimuthal angle
ϕ; ϕ_s	phase of oscillating voltage; synchronous phase

3.1 Introduction

Isochronous cyclotrons are in operation today by the thousands, tens are produced each year. Applications include production of radio-isotopes mostly, proton therapy (Fig. 3.1), high power beams for accelerator-driven systems, secondary particle beam production (Fig. 3.2), and more [1]. The technology and its applications are fostered by cryogeny and high fields which further allow compactness (Fig. 3.1) as well as highest beam rigidities (Fig. 3.3).

Fig. 3.1 COMET proton-therapy cyclotron at PSI. A 250 MeV, 500 nA, 4-sector isochronous AVF cyclotron. The spiral poles enhance axial focusing. A 3 m diameter superconducting coil provides the dipole field [2]

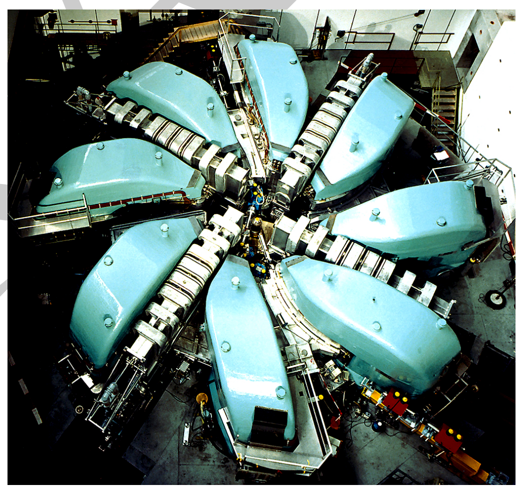

Fig. 3.2 PSI 590 MeV ring cyclotron delivers a 1.4 MW proton beam. Acceleration takes ~180 turns; extraction efficiency is > 99.99%; overall diameter is 15 m. Beam is used for the production of secondary neutron and muon beams [3]

At the origin of the evolution of the cyclotron technology, which led to the AVF innovation in the late 1930s, is the energy limitation of the classical cyclotron, at a few 10s of MeV/nucleon (Chap. 3). Axial focusing in the latter results from the slow decrease of the guiding field with radius in the wide gap between the electromagnet

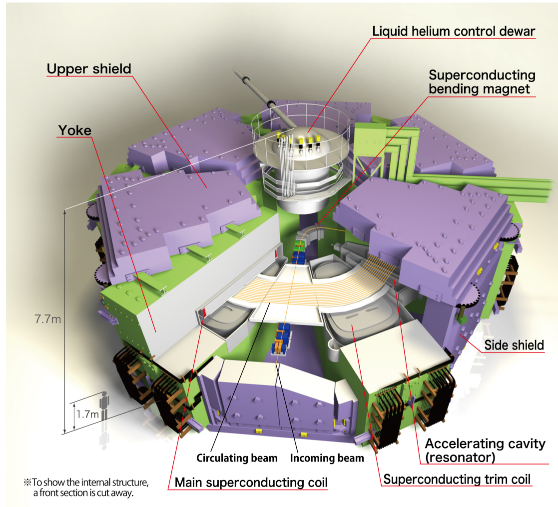

Fig. 3.3 RIKEN K2500, superconducting coil, separated-sector, 8,300 ton ring cyclotron [4]. The dipole field is 3.8 T, rigidity 8 T m, diameter 18.4 m. Beam injection radius is 3.56 m, extraction radius is 5.36 m. The cyclotron is part of a radioactive ion beam accelerator complex [4]

poles. That negative field index $-1 < k < 0$ (Eqs. 3.11, 3.12) results in both radial and axial periodic stability (Eq. 3.18). Isochronism requires instead the field to increase with radius, *i.e.* a field index $k > 0$, a consequence of $B(R) \propto \gamma(R)$ (Sect. 3.2). The AVF concept by L.H. Thomas in 1938[1] [5] (Fig. 3.4), solved the problem:

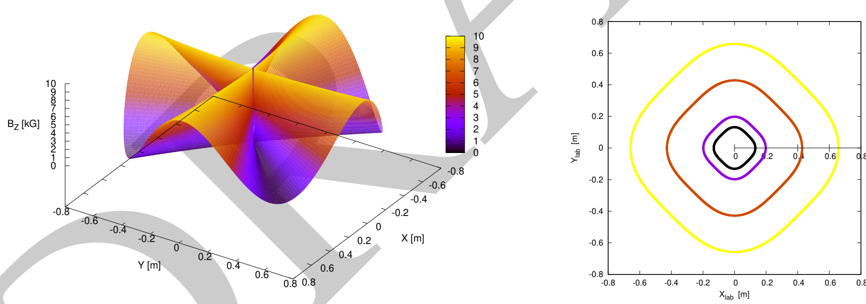

Fig. 3.4 A 4-periodic AVF cyclotron design (after Ref. [5]). Left: mid-plane azimuthally modulated field. Right: closed orbits around the cyclotron feature azimuthally varying curvature, greater on the hills, weaker in the field valleys

AVF entails axial periodic stability as long as the field modulation parameter $F > \beta\gamma$ (Sect. 3.2.1). The vertical defocusing effect which the radially increasing field causes is compensated by the focusing effect of the AVF. Spiral pole geometry was

[1] The very L.H. Thomas of the Thomas-BMT spin motion differential equation, author of the eight years earlier Nature article [7].

further introduced in 1954 [8] to increase axial focusing, so allowing greater k and isochronous acceleration to higher energy (Sect. 3.2.2). It took some time, until the late 1950s (see Stammbach's Fig. 3.4), for Thomas' concept to make its way and lead up to practial realisations[2]. AVF cyclotrons were constructed to accelerate all sorts of ions whereas classical cyclotrons tended to leave the scene (Fig. 3.4). Applications included material science, radiobiology, production of secondary beams, and more. Polarized ion beams became part of the landscape as well from the moment polarized ion sources were made available [10].

The separated sector method was developed in the early 1960s, instances are today's high power PSI 590 MeV spiral sector cyclotron (Fig. 3.2), brought into operation in 1974, and its injector-II, a radial-sector design (Fig. 3.5). Iron-free regions between separated sector dipoles allows room for multiple high-Q RF resonators thus greater turn separation at extraction, for higher efficiency extraction systems and thus higher beam current, and for the insertion of beam instrumentation. Cyclotron energy subsequently increased, up to the present days near-GeV range. Cryogeny was introduced in the early 1960s at the Michigan State University superconducting coil K500 cyclotron[3] [11]. Superconducting technology allows higher field and reduction of size, culminating today with RIKEN's K2500 SRC (Fig. 3.3).

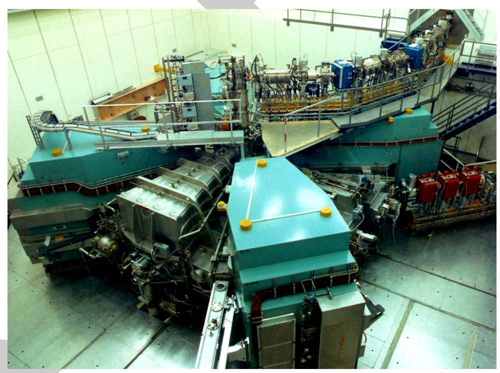

Fig. 3.5 PSI injector II, four separated radial sectors, 0.87 MeV injection energy, accelerates protons to 72 MeV in about 100 turns [6]. The drifts include the 50.7 MHz accelerating RF system and a flattop cavity. Injection is from the top, in the central region

3.2 Basic Concepts and Formulæ

Mass increase with energy causes loss of synchronism in the classical cyclotron, and the required negative field index (decreasing guiding field with radius) for

[2] One can read for instance, in 1959's Ref.[9], Cyclotrons and Synchrocyclotrons, regarding engineering aspects, *"Also, no consideration is given to the AVF cyclotron, since none of this type has reached the advanced design stage"*.

[3] $K = E\ A/Z^2$, with A the number of mass, Z the number of charge, is a measure of the equivalent proton energy, 500 MeV in this case.

Table 3.1 A comparison between an AVF and a separated sector cyclotron of same energy, 72 MeV, namely, the former AVF injector and the present Injector II of PSI high power cyclotron, after Ref. [10, p. 126])

		AVF	separated sector
Injection energy	keV	14	870
Extraction energy	MeV	72	72
Beam current	mA	0.2	1.6
Magnet		single dipole	4 sectors
Weight	ton	470	4×180
Dipole gap height	mm	240 to 450	35
$\langle B \rangle$; $B_{\max}$	T	1.6; 2	0.36; 1.1
RF system		180^o dees	2 resonators
Accelerating voltage	kV	2×70	4×250
RF	MHz	50	50
Normalized beam emittance, hor.; vert.	$\pi\mu$m	2.4; 1.2	1.2; 1.2
Beam phase width	deg	16 - 40	12
Energy spread	%	0.3	0.2
Turn separation at extraction	mm	3	18

axial periodic motion stability adds to the effect. Isochronism instead, *i.e.*, constant $\omega_{\rm rev} = qB/\gamma m_0$, given orbit radius $R = \beta c/\omega_{\rm rev}$, leads to positive index

$$k = \frac{R}{B}\frac{\partial B}{\partial R} = \frac{\beta}{\gamma}\frac{\partial \gamma}{\partial \beta} = \beta^2\gamma^2 \tag{3.34}$$

requiring k to follow the energy increase: the weak focusing condition $-1 < k < 0$ can not be satisfied, transverse periodic stability is lost.

Isochronism requires the revolution period $T_{\rm rev} = 2\pi\gamma m_0/qB$ to be momentum independent; under this condition, differentiating this expression yields the radial field dependence

$$B(R) = \frac{B_0}{\gamma_0}\gamma(R) \tag{3.35}$$

with B_0 and γ_0 some reference conditions,

This led H.A. Bethe and M.E. Rose to conclude, in 1938, *"... it seems useless to build cyclotrons of larger proportions than the existing ones... an accelerating chamber of* 37 *cm radius will suffice to produce deuterons of* 11 *MeV energy which is the highest possible..."* [12]. And F.T. Cole to comment, *"If you went to graduate school in the* 1940*'s, this inequality* $[-1 < r(dB/dr)/B < 0]$ *was the end of the discussion of accelerator theory."* [13, Sect. 1.4].

3.2.1 Thomas Focusing

Whereas the classical cyclotron approach assumed revolution symmetry of the field, a 1938 publication stated: "[...] *a variation of the magnetic field with angle,* [...] *of* *order of magnitude v/c; together with nearly the radial increase of relative amount* $\frac{1}{2}v^2/c^2$ *of Bethe and Rose; gives stable orbits that are in resonance and not defocused."* [5]. In other words, AVF in proper amount (Fig. 3.4) compensates the axial defocusing resulting from the increase of the field with radius (Eq. 3.35). Azimuthal field modulation and radial increase may be obtained by shaping the magnet poles, as illustrated in Fig. 3.6.

Fig. 3.6 Pole shaping in an AVF cyclotron, an electron model, here [14]. The focusing pattern is FfFfFf, an alternation of strong (hill regions) and weak (valleys) radial focusing [15]

Azimuthal field modulation, flutter

A simple approach to the $2\pi/N$-periodic axial symmetry and field modulation may assume a sinusoidal azimuthal form factor

$$\mathcal{F}(\theta) = 1 + f\,\sin(N\theta) \tag{3.36}$$

This is the case in Fig. 3.4, for instance. The mid-plane field can thus be expressed under the form

$$B(R,\theta) = B_0\,\mathcal{R}(R)\,\mathcal{F}(\theta) \tag{3.37}$$

with $\mathcal{R}(R)$ the radial dependence. The orbit curvature varies along the $\frac{2\pi}{N}$-periodic orbit, this requires distinguishing between the local focusing index $n = \frac{\rho(s)}{B(s)}\frac{dB}{d\rho}$ and the geometrical index k (Eq. 3.34), a global quantity which determines the wave numbers (Eq. 3.39). A "flutter" factor can be introduced to quantify the effect of the azimuthal modulation of the field on the focusing,

$$F = \left(\frac{<(\mathcal{F}-<\mathcal{F}>)^2>}{<\mathcal{F}>^2}\right)^{1/2} \ \xrightarrow{\text{hard edge}}\ \left(\frac{R}{\rho}-1\right)^{1/2} \tag{3.38}$$

where $<*>= \oint(*)\,d\theta/2\pi$. If the scalloping of the orbit (*i.e.*, its excursion in the vicinity of R) is of small amplitude, then $R \approx \rho$ and, accounting for the isochronism condition (Eq. 3.34), approximate values of the wave numbers write

$$\nu_R \approx \sqrt{1+k} \overset{\text{isochr.}}{=} \gamma, \qquad \nu_y \approx \sqrt{-k+F^2} \overset{\text{isochr.}}{=} \sqrt{-\beta^2\gamma^2+F^2} \tag{3.39}$$

Thus the horizontal wave number increases during acceleration, linearly with energy, whereas in the absence of countermeasure the axial wave number would decrease - see Sect. 3.2.2. An additional property is

$$\nu_R^2 + \nu_y^2 = 1 + F^2 \quad \xrightarrow{\substack{\text{hard}\\ \text{edge}}} \frac{R}{\rho} \tag{3.40}$$

The flutter allows designing $-k + F^2 > 0$ (whereas $k > 0$), so ensuring periodic stability of the axial motion. In the hypothesis of a sinusoidal azimuthal field modulation (Eq. 3.36) one has $F = f/\sqrt(2)$ and

$$\nu_y \approx \sqrt{-k + f^2/2}, \qquad \nu_R^2 + \nu_y^2 = 1 + f^2/2 \tag{3.41}$$

Off-Momentum Orbit

The dispersion function $D = \delta x/\,\delta p/p$ in the revolution symmetry field is (Eq. 3.20) has the form $D = \frac{R_0}{1+k}$. Given the isochronous condition $k = \beta^2\gamma^2$ it can be written

$$D = \frac{R}{\gamma^2} \tag{3.42}$$

An alternate approach consists in considering that, with the isochronism condition $2\pi R/\beta c = T_{\text{rev}}$, a constant, one gets $\frac{dR}{R} = \frac{d\beta}{\beta} = \frac{1}{\gamma^2}$.

AVF Modeling

A numerical approach to the azimuthal modulation beyond the simple sine modulation of Eq. 3.36, is discussed in Sect. 13.3.3 (Eqs. 13.12, 13.16). It provides a modeling of $\mathcal{F}(\theta)$ over the whole beam excursion area, possibly including an R-dependence, $\mathcal{F}(R,\theta)$. The method ensures the continuity of $\mathcal{F}(R,\theta)$ and its derivatives, between neighboring magnetic sectors. It is resorted to in the simulation exercises.

Wedge Focusing

In the entrance and exit regions of a bending sector, closed orbits are at an angle to the iso-field lines, this causes "wedge focusing", an effect sketched in Fig. 3.7: with positive wedge angle ε, case of the AVF configuration, radial focusing decreases whereas the angle of off mid-plane particle velocity vector to the azimuthal component of the field in the wedge region causes axial focusing.

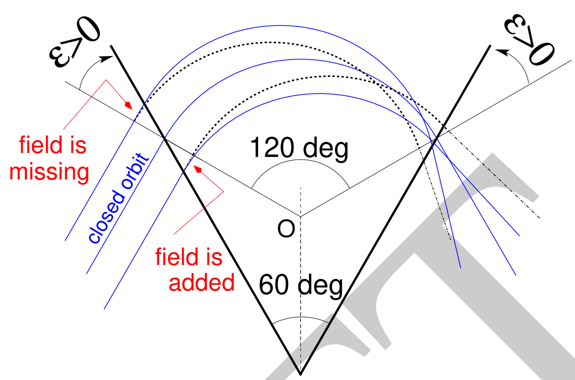

Fig. 3.7 A 120 deg bending of the closed orbit (curvature center at O) is ensured by a 60 deg bending sector. This results in a wedge angle ($\varepsilon > 0$ by convention in this configuration) in the transition regions between valleys and hills, which causes a decrease of the radial focusing (solid incoming trajectories, compared to dotted ones), and axial focusing under the effect of the trajectory angle to the azimuthal field component

3.2.2 Spiral Sector

Spiral sector geometry was introduced in 1954 in the context of fixed field alternating gradient accelerator (FFAG) studies [8], and found application in cyclotrons (as in PSI's COMET cyclotron, Fig. 3.1). Spiraling the edges (Fig. 3.8) results in stronger axial focusing (Eq. 3.45) compared to a radial sector (Eq. 3.39), it also permits an increase of the wedge angle with radius, so maintaining proper compensation of an increase of $k(R)$ (Eq. 3.34). In a spiral sector bend the wedge angle is positive on one side of the sector, negative on the other side (Fig. 3.8), with a global axial focusing resultant. In a similar approach to the periodic field modulation in a radial sector (Eq. 3.36), a convenient approach to the spiral sector AVF uses azimuthal form factor

$$\mathcal{F}(R,\theta) = 1 + f \sin\left[N\left(\theta - \tan(\zeta(R)) \ln\frac{R}{R_0}\right)\right] \tag{3.43}$$

with the spiral angle $\zeta(R)$ an increasing function of radius R, whereas the mid-plane field now writes under the form

$$B(R,\theta) = B_0\, \mathcal{R}(R)\, \mathcal{F}(R,\theta) \tag{3.44}$$

The local magnet edge geometry at R satisfies $r = r_0 \exp(\theta/\tan(\zeta))$, a logarithmic spiral centered at the center of the ring, with ζ the angle between the tangent to the spiral edge and the ring radius (Fig. 3.8). This results in a larger contribution of the flutter term in the axial wave number,

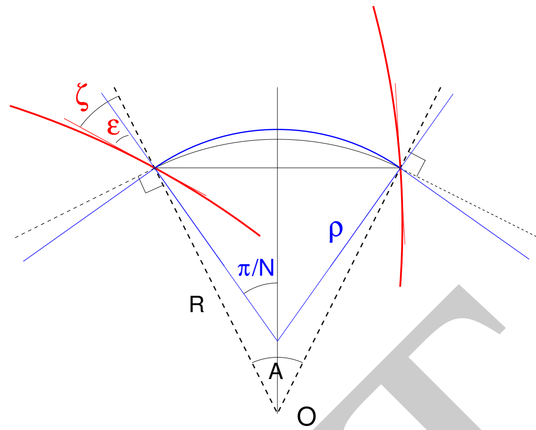

Fig. 3.8 Geometrical parameters of a spiral sector dipole. The center of the ring is at O, ζ is the spiral angle (increasing with radius), ε is the wedge angle. In the hard edge field model, a line of constant field inside the sector is an arc of radius R; thus the curvature radius ρ varies along the closed orbit in the dipole

$$\nu_y \approx \sqrt{-k + F^2(1 + 2\tan^2\zeta)} \tag{3.45}$$

As the field index k increases with R to ensure isochronism (Eq. 3.34), the spiral angle follows so to maintain $-k + F^2(1 + 2\tan^2\zeta) > 0$. A limitation here is the maximum spiral angle achievable, obviously $\zeta \longrightarrow 90$ deg.

As an illustration, in TRIUMF cyclotron ζ reaches 72 deg in the 500 MeV region (from zero in the 100 MeV region) whereas $1 + 2\tan^2\zeta$ increases to 20 (from 1 in the 100 MeV region) and compensates a low $F < 0.07$ (down from $F = 0.3$). In PSI 590 MeV cyclotron ζ reaches 35^o on the outer radius. Most isochronous cyclotrons of a few tens of MeV use spiral sectors to benefit from the more efficient axial focusing [15].

More can be found in the scaling FFAG chapter (Sect. 9.2.2) regarding the spiral sector, and regarding its numerical simulation.

3.2.3 Isochronism

In the hypothesis of isochronism, the revolution angular frequency satisfies $\omega_{\rm rev} = c\beta(\gamma)/R(\gamma) = $ constant. An orbital radius $R_\infty = c/\omega_{\rm rev}$ is reached asymptotically as $\beta = v/c = R/R_\infty \longrightarrow 1$. In terms of the RF and harmonic number,

$$R_\infty = h\frac{c}{\omega_{\rm rf}} \tag{3.46}$$

Given $BR_\infty = \gamma m_0 c/q$ and using $\gamma = \left(1 - (R/R_\infty)^2\right)^{-1/2}$, the radial dependence of the field can be expressed in terms of R_∞, namely,

$$B_0\mathcal{R}(R) = \gamma B_0 = \frac{B_0}{\sqrt{1 - (R/R_\infty)^2}} \qquad \text{with } B_0 = \frac{m_0\omega_{\rm rev}}{q} = \frac{m_0}{q}\frac{\omega_{\rm rf}}{h} \tag{3.47}$$

and goes to infinity with $R \to R_\infty$. For protons for instance, with $m_0/q = 1.6726 \times 10^{-27}[kg]\,/\,1.6021 \times 10^{-19}[C] \approx 10^{-8}$, $BR_\infty[T\,m] = \gamma m_0 c/q \approx 3\gamma$. A typical value for R_∞ can be obtained assuming for instance an upper $\gamma = 1.64$ (600 MeV) in a region of upper field value $B = 1.64$ T, yielding $R_\infty \approx 3$ m.

Radial field

From Eq, 3.47 it results that the radial field form factor of Eqs. 3.37, 3.44 can be written

$$\mathcal{R}(R) = \left(1 - \left(\frac{R}{R_\infty}\right)^2\right)^{-1/2} \tag{3.48}$$

A possible approach consists in using the Taylor expansion of $\mathcal{R}(R)$ (within the limits of radius of convergence of that series), namely

$$\mathcal{R}(R) = 1 + \frac{1}{2}\left(\frac{R}{R_\infty}\right)^2 + \frac{3}{8}\left(\frac{R}{R_\infty}\right)^4 + \frac{5}{16}\left(\frac{R}{R_\infty}\right)^6 + \ldots \tag{3.49}$$

The coefficients in this polynomial in R/R_∞ are the field index and its derivatives, they can be a starting point for further refinement of the isochronism, including for instance side effects of the azimuthal field form factor $\mathcal{F}(R,\theta)$ (Eqs. 3.36, 3.43).

The radial field index $k(R)$ in the AVF cyclotron is designed to satisfy the condition of isochronism (Eq. 3.34). However, reducing the RF phase slip over the acceleration cycle substantially below $\pm\pi/2$ requires a tolerance below 10^{-5} on field value over the orbit excursion area. This tight constraint requires pole machining, shimming, and other correction coil strategies in order to satisfy Eq. 3.34.

Fast Acceleration

Fixed field and fixed RF allow fast acceleration, the main limitation is in the amount of voltage which can be implemented around the ring. The voltage per turn reaches 4 MV for instance at the PSI 590 MeV ring cyclotron, where bunches are accelerated from 72 MeV to 590 MeV in less than 200 turns.

Harmful resonances may have to be crossed as wave numbers vary during acceleration, including the "Walkinshaw resonance" $\nu_R = 2\nu_y$ as $\nu_R \approx \gamma$ whereas the axial wave number spans $\nu_y \approx 1^- \sim 1.5$. This coupling resonance may result in an increase of vertical beam size and subsequent particle losses, fast crossing mitigates the effect.

Fast acceleration improves extraction efficiency, as the turn separation dR/dn is proportional to the energy gain per turn (Sect. 3.2.4).

3.2.4 Cyclotron Extraction

The minimum radial distance between the last two turns, where the extraction septum is located, is imposed by beam loss tolerances, which in some cases (high power beams for instance) may be tight, in the 10^{-4} range or less. Space charge in particular matters, as it increases the energy spread, and thus the radial extent of a bunch. In the relativistic cyclotron the separation between two consecutive turns satisfies

$$\Delta R \approx \frac{\gamma}{\gamma+1}\frac{\Delta E}{E}\frac{R}{\nu_R^2} \tag{3.50}$$

with ΔE the effective acceleration rate per turn. This indicates that greater turn separation at extraction results from increased ring size. As a matter of fact, size is a limitation to intensity in small cyclotrons. It also indicates that extraction efficiency may be increased by moving the radial wave number closer to $\nu_R = 1$.

3.2.5 Resonant Spin Motion

In the quasi-uniform, quasi vertical field $\mathbf{B} \approx \mathbf{B}_y$ of a classical cyclotron dipole, spins quietly perform $G\gamma$ precessions around a vector $\boldsymbol{\omega}_{\rm sp} \parallel \mathbf{B}$ (Eq. 3.30) as the particle velocity completes a 2π precession around the ring (Sect. 3.2.5) [16].

More is liable to happen in the AVF cyclotron, due to the strong radial field index (Eq. 3.34) and to the azimuthal field modulation (Eqs. 3.36, 3.43): the azimuthal and radial field components B_θ and B_R are non-zero out of the median plane, $\mathbf{B}(R, \theta, y)$ may locally depart from vertical in a substantial manner, and so will the local precession vector $\boldsymbol{\omega}_{\rm sp}(R, \theta, y)$. The latter varies periodically in addition, as the particle undergoes periodic vertical motion about the median plane. Resonance between spin precession (characterized by spin tune $\nu_{\rm sp} = G\gamma$, Eq. 3.33) and periodic perturbing field components (characterized by the axial wave number ν_y, Eqs. 3.39, 3.45) occurs if the two motions feature coinciding frequencies. This condition can be expressed under the form

$$\nu_{\rm sp} \pm \nu_y = integer \quad \text{or, equivalently} \quad G\gamma = integer \pm \nu_y \tag{3.51}$$

The spin precession axis $\boldsymbol{\omega}_{\rm sp}$ moves away from the vertical as the spin motion gets closer to resonance (during acceleration as $G\gamma$ varies for instance), to end up in the median plane on the resonance [17, Sect. 3.6].

Consider now an ion bunch, away from any depolarizing resonance. Its polarization is $\langle S_{\rm y}\rangle$, the average of the projection of the spins on the vertical. If a depolarizing resonance is crossed during acceleration, the initial polarization (far upstream of the resonance; index i) and final polarization (far downstream of the resonance; index f) satisfy the Froissart-Stora law [18],

$$\frac{\langle S_{\rm y}\rangle_f}{\langle S_{\rm y}\rangle_i} = 2e^{-\frac{\pi}{2}\frac{|\epsilon_R|^2}{a}} - 1 \tag{3.52}$$

where $|\epsilon_R|$ is the strength of the resonance: a measure of the strength of the depolarizing fields, its calculation is addressed in a next chapter; a is the resonance crossing speed,

$$a = G\frac{d\gamma}{d\theta} \pm \frac{d\nu_y}{d\theta} \tag{3.53}$$

The Froissart-Stora formula indicates that, if the resonance is crossed slowly ($a \to 0$), $\langle S_y \rangle_f / \langle S_y \rangle_i \to -1$: spins quietly follow the flipping motion of the precession axis, polarization is flipped and preserved. If the crossing is fast ($a \to \infty$), $\langle S_y \rangle_f / \langle S_y \rangle_i \to 0$, polarization is unaffected. Intermediate crossing speeds cause polarization loss: $|\langle S_y \rangle|$ ends up smaller after the resonance.

3.3 Exercises

Exercises 3.14 to 3.16 use a field map, designed in exercise 3.13, to simulate an AVF cyclotron dipole. Note that they can be performed using DIPOLE[S] analytical field model instead, as in exercise 3.17 (a similar simulation which can be referred to is exercise 3.2, Classical Cyclotron Chapter). As a reminder, regarding the interest of one or the other of the two methods: field maps allow close to real field models (a measured field map for instance, or from a magnet computer code); using an analytical field model allows more flexibility regarding magnet parameters, which can for instance be optimized using a matching procedure.

Note: some of the input data files for these simulations are available in `zgoubi` sourceforge repository at

[pathTo]/branches/exemples/book/zgoubiMaterial/cyclotron_relativistic/

3.13 Modeling Thomas AVF Cyclotron

Solution: page 367.

In this exercise a 2D mid-plane field map is built, inspired from Thomas's 1938 article [5]. The method to build the map is that of Exercise 3.1, TOSCA[MOD.MOD1=22.1] keyword is used to raytrace through and derive the optical parameters of the 4-period AVF cyclotron.

(a) Construct a 360^o 2D map of the median plane field $B_Z(R,\theta)$, simulating the field in the 4-period Thomas cyclotron of Fig. 3.4, assuming the following:

- $B_Z(R,\theta) = B_0[\,1 + f\sin(4(\theta - \theta_i))\,]$ (Eq. 3.36), with θ_i some arbitrary origin of the azimuthal angle, to be determined. Hint: depending on θ_i value, the closed orbit may be at an angle to the polar radius, as seen in Fig. 3.4; in that case TOSCA[MOD.MOD1=22.1] would require non-zero in and out positioning angles TE and TS, to be determined and stated using KPOS option [19]; instead, a proper choice of θ_i value allows a simpler TE=TS=0;

- an average axial field $B_0 = 0.5$ T on the 200 keV radius (the latter, $R_0(B_0)$, is to be determined), $B_Z > 0$ and $0 < f < 1$ modulation.

- an arbitrary field index k - a good idea is to start building and testing the AVF in the case $k = 0$;

- a uniform map mesh in a polar coordinate system (R, θ) as sketched in Fig. 3.17, covering R=1 to 100 cm; take a radial increment of the mesh $\Delta R = 0.5$ cm, azimuthal increment $\Delta\theta = 0.5\,\mathrm{cm}/R_M$, with R_M some reference radius, say $R_M = 50$ cm, half way between map boundaries;

- an appropriate 6-column formatting of the field map data for TOSCA to read, as follows:

$$R\cos\theta,\ Z,\ R\sin\theta,\ BY,\ BZ,\ BX$$

with θ varying first, R varying second in that list. Z is the vertical direction (normal to the map mesh), so $Z \equiv 0$ in this 2D mesh.

Provide a graph of $B_Z(R, \theta)$ over the extent of the field map.

(b) Raytrace a few concentric closed trajectories centered on the center of the dipole, ranging in $10 \le R \le 80$ cm. Provide a graph of these concentric trajectories in the $(O; X, Y)$ laboratory frame, and a graph of the field along trajectories. Initial coordinates can be defined using OBJET, particle coordinates along trajectories during the stepwise raytracing can be logged in zgoubi.plt by setting IL=2 under TOSCA.

(c) Check the effect of the integration step size on the accuracy of the trajectory and time-of-flight computation, by considering some Δs values in [0.1,10] cm, and energies in a range from 200 keV to a few tens of MeV (considering protons).

(d) Produce a graph of the energy or radius dependence of wave numbers.

(e) Calculate the numerical value of the axial wave number, ν_y, from the flutter (Eqs. 3.38, 3.39). Comparing with the numerical values, discrepancy is found: repeat (d) for f=0.1, 0.2, 0.3, 0.6, check the evolution of this discrepancy.

3.14 Designing an Isochronous AVF Cyclotron

Solution: page 375.

(a) Introduce a radius dependent field index $k(R)$ in the AVF cyclotron designed in exercise 3.13, proper to ensure R-independent revolution period, in three different cases of modulation: f=0 (no modulation), f=0.2 and f=0.9.

Check this property by computing the revolution period T_{rev} as a function of kinetic energy E_k, or radius R. On a common graph, display both T_{rev} and $dT_{\mathrm{rev}}/T_{\mathrm{rev}}$ as a function of radius, including for comparison a fourth case: B=constant=5 kG.

(b) Provide a graph of the energy dependence of wave numbers.

3.15 Acceleration to 200 MeV in an AVF Cyclotron

Solution: page 380.

In this exercise protons are accelerated to over 100 MeV in an AVF cyclotron: well beyond the about 20 MeV energy reached in the classical cyclotron (see exercise 3.10).

(a) Produce an acceleration cycle of a proton, from 0.2 to 100 MeV, in the AVF cyclotron designed in exercise 3.14. Note that a dedicated field map has to be created in order to allow for the higher maximum energy - a 3 meter field map outer radius works. Assume proper modulation coefficient f for axial focusing all the way to

300 MeV. Assume a double-dee design, and 400 keV peak voltage in the gap, use CAVITE[IOPT=7] for acceleration to account for RF phase.

(b) Give a graph of the energy dependence of wave numbers over the acceleration range.

3.16 Thomas-BMT Spin Precession in Thomas Cyclotron

Solution: page 384.

This exercise uses the field maps and input data file of exercise 3.15. Dependence of energy boost on RF phase is removed by using CAVITE[IOPT=3] [19]. Consider helion ions: use PARTICUL[Name=HELION] to define mass, charge and G factor, all quantities needed for the integration of Thomas-BMT differential equation (Eq. 3.30).

(a) By scanning the axial wave number, find the $G\gamma$ value for which the spin motion resonance condition (Eq. 3.51) is satisfied.

(b) Consider a particle with non-zero axial motion, so that it experiences horizontal magnetic field components as it circles around. Track its spin through the resonance, take initial spin vertical $\mathbf{S} \equiv \mathbf{S}_Z$. Provide a graph of S_Z as a function of $G\gamma$ or energy.

(c) Simulate resonance crossing for a series of different vertical motion amplitudes Z_0; produce a graph of these resonance crossings $S_Z(turn)$.

Plot the ratio $S_{\mathrm{y,f}}/S_{\mathrm{y,i}}(Z_0)$. From a match of this $S_{\mathrm{y,f}}/S_{\mathrm{y,i}}$ series with Eq. 3.52, show that the resonance strength changes in proportion to the vertical excursion.

(d) Repeat (c) for a series of different resonance crossing speeds instead (Eq. 3.53), leaving Z_0 unchanged.

Show that this $S_{\mathrm{y,f}}/S_{\mathrm{y,i}}$ series can be matched with Eq. 3.52.

3.17 Isochronism and Edge Focusing in a Separated Sector Cyclotron

Solution: page 387.

This exercise uses DIPOLE to simulate a 30 deg sector dipole of a 4-period cyclotron, and allow playing with field fall-off extent at dipole EFBs. The configuration of the cyclotron is typically that of PSI 72 MeV injector (Fig. 3.5). DIPOLE allows radial field indices up to the third order ($\partial^3 B_Z/\partial R^3$) [19, Eq. 6.3.18]. In question (b) however, higher order indices are needed to improve the isochronism, requiring the use of DIPOLES [19, Eqs. 6.3.20, 21].

Take fringe fields into account (see Sect. 13.3.3), with

- λ = 7 cm the fringe extent (changing λ changes the flutter, Eq. 3.38),

- $C_0 = 0.1455$, $C_1 = 2.2670$, $C_2 = -0.6395$, $C_3 = 1.1558$ and $C_4 = C_5 = 0$, for a realistic field fall-off model.

(a) Assume $k = 0$, here. Produce a model of a period using DIPOLE.

Produce a graph of closed orbits across a period for a few different rigidities (FIT can be used to find them), and a graph of the field along these orbits.

(b) In this question, R-dependence of the mid-plane magnetic field proper to ensuring energy independent revolution period is introduced. Use DIPOLES here, as it allows b_i field indices to higher order, as necessary to reach tight isochronism over the full energy range.

Assume a peak field value $B_0 = 1.1$ T at a radius of 3.5 m in the dipoles. Find the average orbit radius R, and average field B (such that $BR = p/q$), at an energy of 72 MeV.

Determine a series of index values, $b_{\mathrm{i=1,n}}$, in the model [19, Eq. 6.3.19]

$$B_Z(R,\theta) = B_0\,\mathcal{F}(R,\theta)\left(1 + b_1\frac{R-R_0}{R_0} + b_2\left(\frac{R-R_0}{R_0}\right)^2 + \ldots\right) \qquad (3.54)$$

proper to bring the revolution period closest to R-independent, in the energy range 0.9 to 72 MeV (hint: use a Taylor development of Eq. 3.48 and identify with the R-dependent factors in Eq. 3.54).

(c) Play with the value of λ, concurrently to maintaining isochronism with appropriate b_i values. Check the evolution of radial and axial focusing - OBJET[KOBJ=5] and MATRIX[IORD=1,IFOC=11] or TWISS, or OBJET[KOBJ=6] and MATRIX[IORD=2,IFOC=11], can be used to get the wave numbers.

From raytracing trials, observe that (i) the effect of λ on radial focusing is weak (a second order effect in the particle coordinates); (ii) greater (smaller) λ value results in smaller (greater) flutter and weaker (stronger) axial focusing (a first order effect). Note: the integration step size in DIPOLE[S] has to be consistent with the field fall-off extent (λ value), in order to ensure that the numerical integration is converged.

(d) For some reasonable value of λ (normally, about the height of a magnet gap, say, a few centimeters), compute $F^2 = \frac{\left\langle (B(\theta) - <B>)^2 \right\rangle}{<B>^2}$. Check the validity of $\nu_y = \sqrt{-\beta^2\gamma^2 + F^2}$ (Eq. 3.39). OBJET[KOBJ=5] and MATRIX[IORD=1,IFOC=11] can be used to compute ν_y, or multiturn raytracing and a Fourier analysis.

(e) Check the rule $F^2 \stackrel{\text{hard edge}}{\longrightarrow} \frac{R}{\rho} - 1$ (Eq. 3.38), from the field $B(\theta)$ delivered by DIPOLES. Give a theoretical demonstration of that rule.

3.18 A Model of PSI Ring Cyclotron Using CYCLOTRON

Solution: page 390.

The simulation input data file in Tab. 3.2 is based on the use of CYCLOTRON, to simulate a period of the eight-sector PSI ring cyclotron and work on the isochronism. That file is the starting point of the present exercise.

(a) With `zgoubi` users' guide at hand, explain the signification of the data in that simulation input data file.

(b) Compute and plot a few trajectories and field along, across the sector. Provide a graph of field density over the sector.

(c) Compute and plot the radius dependence of the revolution period.

(d) The field indices $b_1,\ b_2, \ldots$ are aimed at realizing the isochronism; four, $b_1 - b_4$ are accounted for in (a) and (b), they were drawn from the PSI cyclotron spiral sector magnet field map data. Question (c) proves this small set of indices to result in a poor isochronism of the orbits.

Table 3.2 Simulation input data file: a period of an eight-sector PSI-style cyclotron. The data file is set up for a scan of the periodic orbits, from radius R=204.1171097 cm to R=383.7131468 cm, in 15 steps

```
PSI CYCLOTRON

'OBJET'
1249.382414
2
1 1
204.1171097  8.915858372  0.  0.  0.  1.  'o'
1
'PARTICUL'
PROTON

'CYCLOTRON'
2
1   45.0  276.  1.0
0. 0. 0.99212277 51.4590015 0.5 800. -0.476376328 2.27602517e-03 -4.8195589e-06 3.94715806e-09
18.3000E+00  1.  28. -2.0
8 1.1024358 3.1291507 -3.14287154 3.0858059 -1.43545 0.24047436 0. 0. 0.
11.0  3.5 35.E-3  0.E-4 3.E-8 0. 0. 0.
18.3000E+00  1.  28. -2.0
8 0.70490173 4.1601305 -4.3309575 3.540416 -1.3472703 0.18261076 0. 0. 0.
-8.5  2.  12.E-3 75.E-6 0.    0. 0. 0.
0. -1
0  0.  0.  0.  0.  0.  0.  0.
0.  0.  0.   0.  0.  0.
2  10.
0.4
2 0.  0. 0.  0.

'FIT2'
2
1 31 0 [-300.,100]
1 35 0 [.1,3.]
2
3.1 1 2 #End 0. 1. 0
3.1 1 3 #End 0. 1. 0
'FAISCEAU'

'FAISTORE'
orbits.fai
1

'REBELOTE'
14 0.2  0 1
1
OBJET 30 221.065356:383.7131468

'SYSTEM'
1
gnuplot <./gnuplot_orbits.gnu
'END'
```

Add higher order indices, until a sufficient number, with proper values, is found that allows FIT to reach a final isochronism improved by an order of magnitude. Provide a revised input data file with updated index series and their values.

References

1. A link to accelerator conference proceedings and its search tool: https://www.jacow.org/Main/Proceedings
2. J.M. Schippers, J.M.: The Superconducting Cyclotron and Beam Lines of PSI's New Proton Therapy Facility "PROSCAN". 17th International Conference on Cyclotrons and their Applications: Tokyo, Japan; 18-22 October 2004. http://accelconf.web.cern.ch/c04/data/CYC2004_papers/20B2.pdf. Copyrights under license CC-BY-3.0, https://creativecommons.org/licenses/by/3.0; no change to the material

3. Seidel, M.: Production of a 1.3 Megawatt Proton Beam at PSI. Proceedings of IPAC'10, Kyoto, Japan, TUYRA03.
http://accelconf.web.cern.ch/IPAC10/talks/tuyra03_talk.pdf. Copyrights under license CC-BY-3.0, https://creativecommons.org/licenses/by/3.0; no change to the material
4. Kawaguchi, T., et al., Design of the sector magnets for the RIKEN superconducting ring cyclotron, Proceedings of the 15th International Conference on Cyclotrons and their Applications, Caen, France.
https://accelconf.web.cern.ch/c98/papers/b-14.pdf
Figure 3.3: the picture, and the permission to use it in this publication, have been granted by RIKEN (January 2023)
5. Thomas, L.H.: The Paths of Ions in the Cyclotron. Phys. Rev. 54, 580, (1938)
6. Joho, Werner: Potential of cyclotrons. https://indico.in2p3.fr/event/115/timetable/?print=1&view=standard
7. Thomas, L.H.: Motion of the spinning electron. Nature. 117 (2945): 514 (1926)
8. Symon, K.R., et al.: Fixed-Field Alternating-Gradient Particle Accelerators. Phys. Rev. 103, 1837 (1956)
9. Cohen, L.B.: Cyclotrons and Synchrocyclotrons. In Encyclopedia of Physics, Vol. XLIV, Nuclear Instrumentation I. Editor S. Flūgge. Springer-Verlag, 1959
10. Stammbach, T.: Introduction to Cyclotrons. CERN accelerator school, cyclotrons, linacs and their applications, IBM International Education Centre, La Hulpe, Belgium, 28 April-5 May 1994. Copyright/License CERN CC-BY-3.0 - https://creativecommons.org/licenses/by/3.0
11. Miller, P.S., et al.: The Magnetic Field of the K500 Cyclotron at MSU Including Trim Coils and Extraction Channels. Procs. 9th Int. Conf. on Cyclotrons and their Applications, September 1981, Caen, France.
http://accelconf.web.cern.ch/c81/papers/ep-05.pdf
12. Bethe, H.A. and Rose, M.E., Phys. Rev. 54, 588 (1938)
13. Cole, F.T.: A memoir of the MURA years. April 11, 1994.
https://epaper.kek.jp/c01/cyc2001/extra/Cole.pdf
14. © The Regents of the University of California, Lawrence Berkeley National Laboratory
15. Craddock, M.K.: AG focusing in the Thomas cyclotron of 1938, Proceedings of PAC09, Vancouver, BC, Canada, FR5REP1.
http://accelconf.web.cern.ch/PAC2009/papers/fr5rep113.pdf
16. Méot, F.: Spin Dynamics. In: Polarized Beam Dynamics and Instrumentation in Particle Accelerators, USPAS Summer 2021 Spin Class Lectures, Springer Nature, Open Access (2023).
https://link.springer.com/book/10.1007/978-3-031-16715-7
17. Méot, F.: Spinor Methods. In: Polarized Beam Dynamics and Instrumentation in Particle Accelerators, USPAS Summer 2021 Spin Class Lectures, Springer Nature, Open Access (2023).
https://link.springer.com/book/10.1007/978-3-031-16715-7
18. Froissart, M., Stora, R.: Depolarisation d'un faisceau de protons polarises dans un synchrotron. Nuclear Instruments and Methods. 7 (3): 297-305 (June 1960)
19. Méot, F.: Zgoubi Users' Guide.
https://www.osti.gov/biblio/1062013-zgoubi-users-guide Sourceforge latest version:
https://sourceforge.net/p/zgoubi/code/HEAD/tree/trunk/guide/Zgoubi.pdf